Topological Stone-Wales Defects Enhance Bonding and Electronic Coupling at the Graphene/Metal Interface

Benedikt P. Klein[1,2,5], Alexander Ihle[3], Stefan R. Kachel[1], Lukas Ruppenthal[1], Samuel J. Hall[4,5], Lars E. Sattler[6], Sebastian M. Weber[6], Jan Herritsch[1], Andrea Jaegermann[1], Daniel Ebeling[3], Reinhard J. Maurer[5], Gerhard Hilt[6], Ralf Tonner-Zech[1†], André Schirmeisen[3*], J. Michael Gottfried[1*]

[1]*Fachbereich Chemie, Philipps-Universität Marburg, Hans-Meerwein-Straße. 4, 35032 Marburg, Germany*

[2]*Diamond Light Source, Harwell Science and Innovation Campus, Didcot, OX11 0DE, United Kingdom*

[3]*Institut für Angewandte Physik, Justus-Liebig-Universität Gießen, Heinrich-Buff-Ring 16, 35392 Gießen, Germany*

[4]*MAS Centre for Doctoral Training, Senate House, and* [5]*Department of Chemistry, University of Warwick, Gibbet Hill Road, Coventry, CV4 7AL, United Kingdom*

[6]*Institut für Chemie, Carl von Ossietzky Universität Oldenburg, Carl-von-Ossietzky-Straße. 9-11, 26111 Oldenburg, Germany*

[†]*Current address: Wilhelm-Ostwald-Institut für Physikalische und Theoretische Chemie, Universität Leipzig, Linnéstraße 2, 04103 Leipzig, Germany*

Abstract

Defects play a critical role for the functionality and performance of materials, but the understanding of the related effects is often lacking, because the typically low concentrations of defects make them difficult to study. A prominent case are the topological defects in two-dimensional materials such as graphene. The performance of graphene-based (opto-)electronic devices depends critically on the properties of the graphene/metal interfaces at the contacting electrodes. The question of how these interface properties depend on the ubiquitous topological defects in graphene is of high practical relevance, but could not be answered so far. Here, we focus on the prototypical Stone-Wales (S-W) topological defect and combine theoretical analysis with experimental investigations of molecular model systems. We show that the embedded defects undergo enhanced bonding and electron transfer with a copper surface, compared to regular graphene. These findings are experimentally corroborated using molecular models, where azupyrene mimics the S-W defect, while its isomer pyrene represents the ideal graphene structure. Experimental interaction energies, electronic-structure analysis, and adsorption distance differences confirm the defect-controlled bonding quantitatively. Our study reveals the important role of defects for the electronic coupling at graphene/metal interfaces and suggests that topological defect engineering can be used for performance control.

Keywords

Graphene, a single atomic layer of graphite, is a versatile material with diverse and technologically important properties, such as high electrical and thermal conductivity, mechanical strength, optical transparency, and chemical inertness.[1] The physico-chemical properties of the ideal graphene lattice are strongly modified by topological defects,[2] which occur intrinsically *e.g.* as point[3-5] or line defects[6-9] at grain boundaries. Defects influence the chemical reactivity,[10-11] mechanical strength,[9, 12-14] electron transport,[6, 15] and magnetism[16] of the graphene layer. Defects can also be introduced artificially to tailor the properties of the graphene sheet through topological design.[17]

Application in (opto-)electronic devices requires contacting the graphene-based active element by metal electrodes.[18] The resulting graphene/metal interface determines the performance of the devices.[19] It has been proposed that defects play a decisive role in the graphene/metal interaction and therefore largely determine the interface properties.[20] However, top- and bottom metal contacts of graphene have only been studied for the ideal graphene lattice, neglecting the influence of topological defects.[21] On the experimental side, the scarcity of related work is due to methodological challenges: Interaction energies, vertical bond distances, or spectroscopic electronic-structure data can often only reliably be obtained with laterally integrating techniques, which do not allow to distinguish contributions of the defects from those of the surrounding ideal graphene lattice.
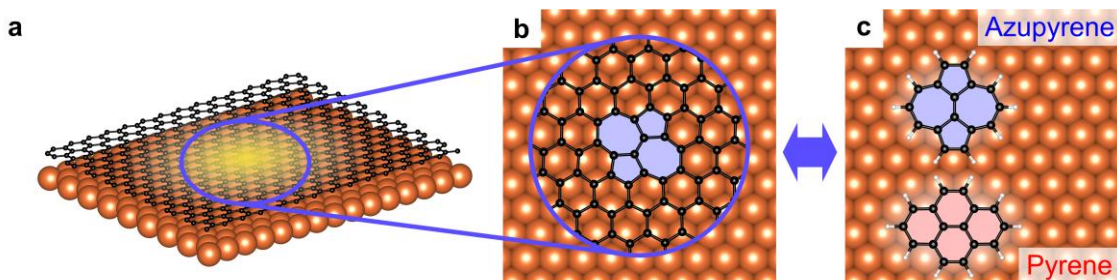

Figure 1. Molecular model systems are chosen according to the topology of the ideal graphene lattice and embedded defects (a). Graphene/metal interface with topological defect (b,c). The local interaction of a topological Stone-Wales (S-W) graphene defect with a metal surface (b) is investigated by a combination of computational and experimental methods applied to embedded defects and related molecular model systems (c). These model systems provide access to information that cannot be obtained for the embedded defects.

To overcome these difficulties, we combine theoretical studies of defect-containing graphene/-metal contacts with experiments using a model system that mimics the local chemical and physical properties of the defect/metal contact, but can be prepared laterally uniform and in high concentration. Specifically, we approximate the Stone-Wales (S-W) defect by the nonbenzenoid aromatic hydrocarbon azupyrene, which has the same topology of the carbon skeleton with two pentagons and two heptagons (5-7-5-7 topology) (Figure 1). The use of a molecular system to represent the defect embedded in the periodic graphene structure assumes

that the topology itself plays a crucial role in the interaction with the substrate. Our calculations of the charge transfer from the metal substrate to the graphene (see below) showed the interaction to be localized at the defect site. Therefore, it seems valid to study the localized interaction of an isolated model defect with the metal substrate and transfer the results toward the embedded defects. It is true that choosing larger polycyclic aromatic molecules (nanographenes) as model systems would increase the comparability with the embedded defect, as well as with the ideal graphene layer. However, it is imperative for the model system to be small enough to employ molecular surface science techniques to gain additional information which cannot be obtained for graphene. In particular, our molecules can thermally desorb, therefore enabling us to quantify their interaction with the surface using temperature programmed desorption.

The S-W defect was chosen because it is a prototypical and ubiquitous intrinsic point defect of graphene and carbon nanotubes.[22-24] As a reference representing the topology of regular graphene, we use the benzenoid isomer of azupyrene, pyrene, which consists only of 6-membered rings (6-6-6-6 topology). In contrast, the 5-7-5-7 topology of azupyrene is classified as nonalternant[25] and is known to strongly influence its electronic structure.[26-27] In related previous work, we compared the two-ring nonbenzenoid aromatic hydrocarbon azulene (5-7 topology) to its benzenoid isomer naphthalene (6-6 topology) regarding their interaction with Cu(111), Ag(111) and Pt(111) surfaces and found that the former binds stronger to all three surfaces.[28-31] Considering the structural analogy, we therefore proposed that nonbenzenoid defect sites in graphene may induce enhanced graphene/metal interactions. However, these previous studies were lacking in two essential points: first, the azulene motif rarely occurs as isolated defect and thus azulene is not a representative model system. And second, these studies did not include any consideration of the graphene-embedded defect, making them rather speculative with respect to the graphene/metal interaction.

Here, we address both shortcomings of the previous work: the first by using azupyrene as a model for the abundant S-W defect, and the second by including a detailed theoretical study of the embedded defects. We find that S-W defects engage in increased electronic interaction with a copper (111) surface, compared to regular graphene. At the S-W defect site, our density functional theory (DFT) calculations show localized electron transfer from the metal to the graphene sheet. The presence of the S-W defect leads to an overall reduced graphene-metal distance and to an increased binding energy. All these results are experimentally corroborated on a qualitative level by the molecular model system.

Results and Discussion

Interface interaction of embedded graphene defects. Figure 2a-c shows the free-standing optimized structures of the ideal graphene lattice, the embedded S-W defect, and an embedded

5-7 defect as predicted by dispersion-corrected periodic DFT calculations. The three different graphene structures were placed on a four-layer Cu(111) slab and optimized in a commensurate superstructure.[32] While the main object of our study is the S-W defect, we also performed calculations for the 5-7 defect, because it is the smallest possible unit with the 5-7 topology and therefore an interesting comparison for the S-W defect.

The defect/metal interaction causes substantial charge redistribution, as shown by the overlayed charge density difference plots in Figure 2d-i. The ideal graphene lattice (Figure 2d,g), undergoes minor charge rearrangement mostly by electron flow from graphene's π-system and from the first copper layer into the interface region. Both defect structures show an additional strong, localized charge transfer around the defects. Note that the charge density rearrangement around the S-W defect in Figure 2e does not reflect the mirror symmetry of the defect. This is attributed to influences of the underlying Cu surface, which does not have the same local symmetry as the defect. The charge transfer was quantified using various charge partitioning schemes (Supplementary Tab. S1), which all show substantial, localized electron transfer from the metal to the graphene defects.
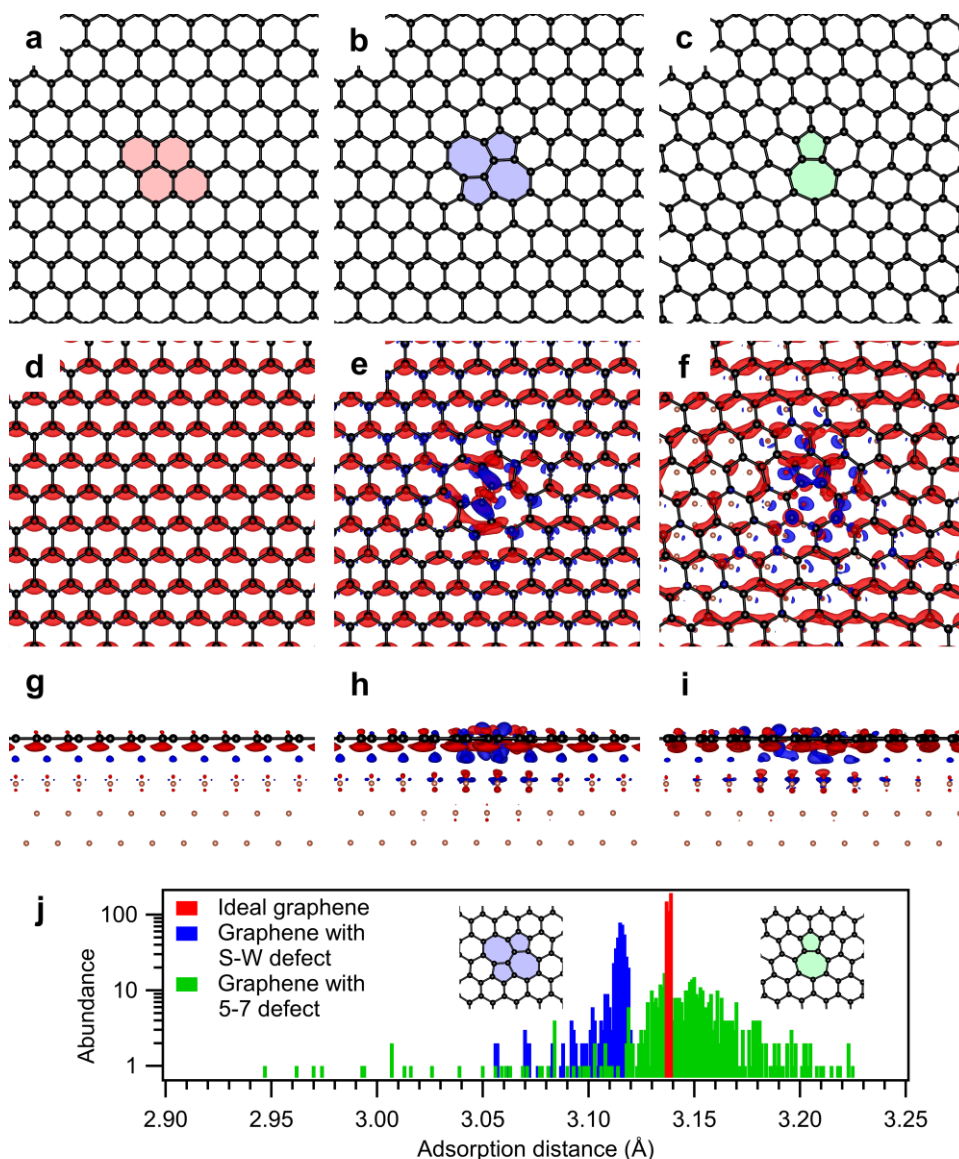
Figure 2. Interaction of topological graphene defects with the Cu(111) surface. Left: ideal graphene lattice, center: with embedded S-W defect, right: with embedded 5-7 defect. (a-c) Optimized structures of the free-standing graphene lattices. (e-f) Top views and (g-i) side views of the charge density difference plots for the three graphene structures adsorbed on Cu(111), isosurface value: 0.0005 e$^-$/Å^3, blue: electron accumulation, red: electron depletion. (j) Abundance distribution for the adsorption heights of the carbon atoms above the Cu(111) substrate. Red, ideal graphene; blue, graphene with S-W defect; green, graphene with 5-7 defect. Large unit cells with 456 carbon atoms were chosen to reduce the lateral interaction between neighboring defects (see Supplementary Figure S1).

The optimized structures also reveal defect-induced changes of the graphene/metal bonding distances. As shown in Figure 2j, the S-W defect (blue histogram) pulls the whole graphene lattice closer to the metal, while the atoms constituting the defect are only slightly closer to the

surface than the rest of the lattice (heights below 3.09 Å in the blue histogram in Figure 2j). For comparison, the 5-7 defect causes substantial corrugation of the graphene sheet, resulting in a much wider spread of the graphene/metal bonding distances (green histogram in Figure 2j). This structure has a larger average height than the ideal graphene lattice, because the strong lateral and vertical distortion around the defect makes carbon atoms occupy unfavorable sites on the metal surfaces. The vertical distortion is partly caused by the required periodicity of the overall structures, while the lateral distortion is one of the reasons why 5-7 defects rarely occurs isolated in the real graphene lattice, but instead form annulated chains at rotational domain boundaries.[7]

Despite the substantial local charge transfer, the graphene/metal interaction energy of the unit cell with the S-W defect is increased by only 6 kJ/mol, compared to ideal graphene, because the distortion-induced registry impairment counteracts the increased bonding. This effect is even stronger for the highly distorted lattice with the 5-7 defect, which weakens the interaction by 35 kJ/mol.

The DFT calculations thus predict defect-induced modifications of the interaction between graphene and a contacting metal surface. Especially the S-W defect causes reduced graphene/metal distances, larger interaction energy, and enhanced electronic interaction with substantial charge transfer. Figure 2e,h clearly shows the charge transfer, which represents a crucial measure for the electronic coupling with the metal surface, to be localized at the defect site. It is not possible to obtain related experimental data on a quantitative level for graphene with embedded defects. However, due to the localized nature of the defect/metal interaction, we are able to circumvent the problem by substituting the defect and the ideal graphene lattice with the molecular model systems and investigating their interaction with the Cu(111) surface. Various experimental and theoretical methods applied to the azupyrene/pyrene pair of isomers prove that the model defect forms the stronger bond to the metal, undergoes pronounced adsorption-induced changes in the electronic structure, and has a significantly shorter adsorption distance.

Structure and bond lengths. The constant-height AFM images of azupyrene (Figure 3a) and pyrene (Figure 3b) reveal the atomic structure of the adsorbed molecules. We determined the precise adsorption positions and conformations (see Supplementary Figure S2 and S3), which agree with our DFT calculations (Figure 3f-m). The topography scanlines for pyrene (red and orange lines in Figure 3d and 3e) reveal a rather flat conformation. The molecule is not curved or bent and only shows a slight apparent tilt along the long molecular axis (red line in Figure 3e), which may be explained by a mismatch between the Cu(111) lattice and the molecular dimensions (Supplementary Figure S2).[33] In contrast, azupyrene assumes a non-tilted, slightly bowl-shaped conformation, where the two central C atoms are approximately 15 pm closer to the Cu(111) surface than the perimeter atoms.
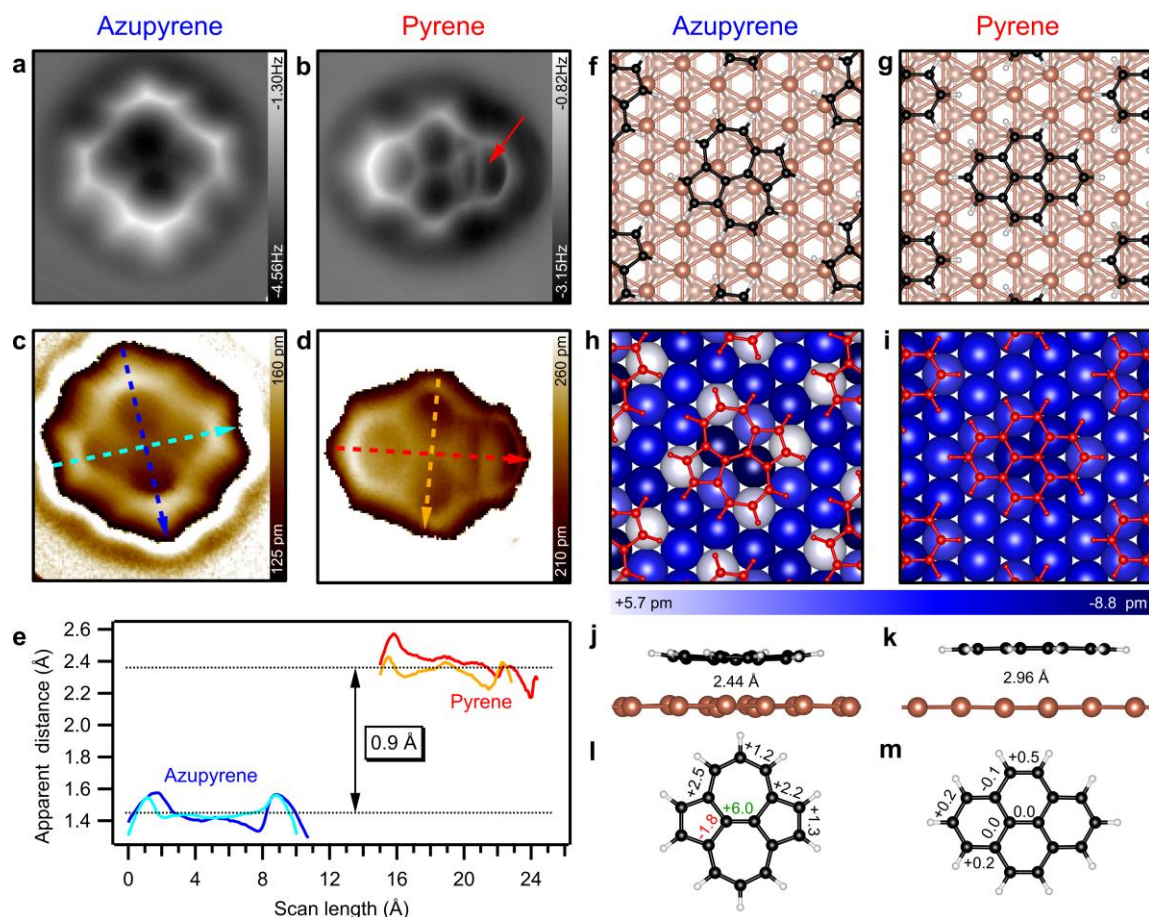
Figure 3. Low-temperature (LT) AFM measurements revealing the chemical structure and the apparent adsorption distances of model defect (azupyrene) and reference (pyrene) on Cu(111) in agreement with DFT calculations. (a,b) Constant-height frequency shift AFM images of azupyrene and pyrene at z = -100 pm (a) and z = -50 pm (b) with respect to a tunneling set point of U = 100 mV and I = 20 pA. The bright vertical line (red arrow) and elongation of the right-hand ring of the pyrene molecule are an image artifact due to tip-induced movements of the molecule (see Supplementary Figure S2 and Supplementary Discussion for details). (c,d) Reconstructed topography images (i.e., adsorption distance) of pyrene and azupyrene obtained from a 3D grid measurement of $\Delta f(z)$-spectra (see Supplementary Figures S2-S4 for details). **e**, Topography scan lines of azupyrene (blue, cyan) and pyrene (red, yellow) showing the difference in the apparent adsorption distance of the molecules. The scan lines are taken along the dashed arrows in c,d. (f,g) Top views of the DFT optimized adsorbate structures. (h,i) vertical displacements (in pm) of the topmost copper atoms, compared to the relaxed clean surface. Positive values (lighter shades of blue) indicate displacement towards the molecule. (j,k) Side views with the calculated vertical bonding distances. (l,m) Interaction-induced changes of the carbon-carbon bond lengths relative to the gas-phase structure (in pm).

According to the apparent average adsorption distances, azupyrene is closer to the surface than pyrene by about 0.9 Å (Figure 3e), indicating stronger interaction of azupyrene with the Cu(111) surface. The measured difference in adsorption distance is larger than the DFT value of 0.52 Å, but this deviation between AFM and DFT distances is in line with previous work both in general[34] and on related systems.[28] For azulene (chemisorbed) and naphthalene (physisorbed) on Cu(111), the comparison of the adsorption distances obtained using AFM, DFT, and normal-incidence X-ray standing wave (NIXSW) measurements showed similar trends: AFM (0.92 Å) and DFT (0.63 Å) provided the largest and smallest differences, respectively, while NIXSW (0.74 Å) yielded an intermediate value.[28]

Molecule-metal interaction energies. Temperature Programmed Desorption (TPD) measurements provide quantitative information about the strength of molecule-metal interactions, if the adsorbate desorbs intact and adsorption is nonactivated.[35] Then, the desorption energy, E_{des}, is a good approximation for the negative differential interaction energy.[36] Figure 4a shows TPD traces for azupyrene and pyrene on Cu(111). For both molecules, the initial coverage for one trace was one monolayer (1 ML, see Methods section for definition), while the second trace corresponds to a 0.06 ML coverage for pyrene and about 0.6 ML for azupyrene.

The pyrene monolayer desorbs completely from the Cu(111) surface, according to XPS. In contrast, desorption of azupyrene occurs only above a residual coverage of 0.53 ML (Supplementary Figure S5). As shown in Figure 4a, the edge of the TPD trace for the lowest desorbing coverage of azupyrene is at 630 K, which is considerably higher than in the case of pyrene (500 K) and thus qualitatively indicates stronger interaction of azupyrene with the metal surface.[30, 37-38]

Quantitative TPD analysis using two independent methods (see Supplementary Methods and Supplementary Figure S7) reveals a pronounced coverage-dependence of E_{des} due to repulsion between the adsorption-induced interface dipoles. Most suitable for the assessment of molecule-metal interaction strengths is the low-coverage range, where repulsion is weakest. The lowest azupyrene coverage where TPD is feasible is 0.53 ML. At this coverage, E_{des} is 198 kJ/mol for azupyrene and 130 kJ/mol for pyrene, indicating that the former binds stronger (+52%) to the metal. Considering the different slopes of the energy curves in Figure 4b, it can be assumed that this difference increases further towards lower coverages, where the desorption of azupyrene is prevented by its strong bond to the metal.
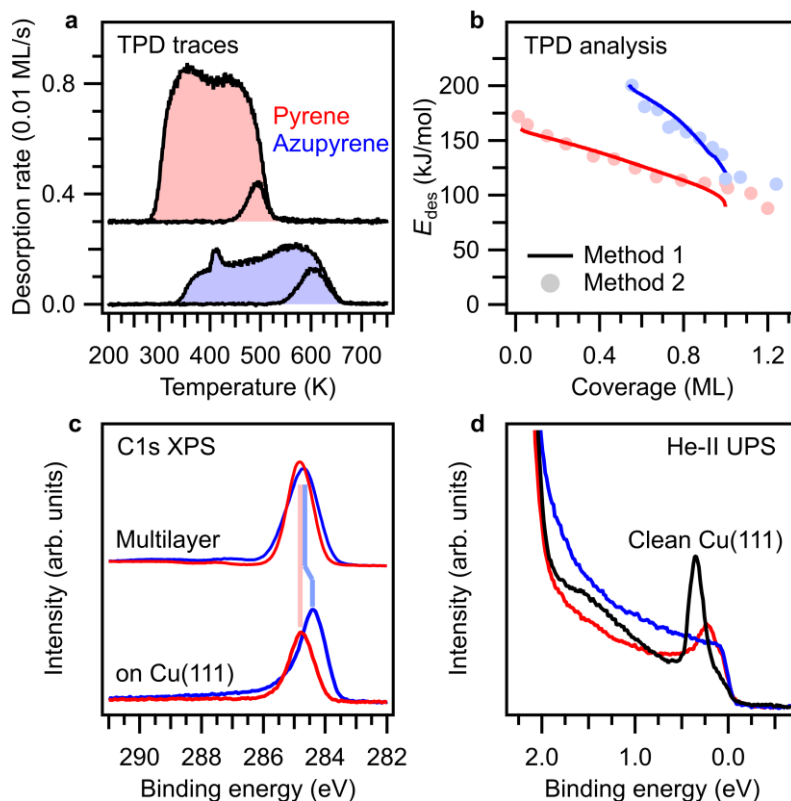
Figure 4. TPD and photoemission (XPS, UPS) data indicating enhanced bonding between the model defect and the metal. (a) TPD traces of azupyrene and pyrene both for initial monolayer coverage and a lower initial coverage. See Supplementary Figure S6 for the TPD data of the intermediate coverages also used in the analysis. (b) Coverage-dependent desorption energies obtained by analysis of the TPD data with two different methods (see the Supplementary Methods). (c) C1s photoemission spectra for multilayers and monolayers on Cu(111). The relative shifts between the two are marked by shaded lines. The asymmetry of the peak for the azupyrene monolayer indicates hybridization with the metal states of the surface. (d) He-II UP spectra of the clean surface (black) and monolayers of azupyrene and pyrene. The disappearance of the surface state (binding energy of 0.3 eV on the clean surface) shows a stronger interaction for azupyrene.

Electronic structure. The interaction-related differences of the adsorbate structures and bond energies correspond to differences in the electronic structures, which are revealed by probing the occupied electronic states with photoemission spectroscopy (XPS, UPS). They enable us to discriminate between van-der-Waals dominated physisorption and chemisorption, because only the latter is associated with significant modifications of the electronic structure.[39]

First, we compare C1s photoemission spectra of multilayers and monolayers (Figure 4c). The multilayer spectra, which probe molecules *not* in direct contact with the metal surface, are

similar for both molecules. The minor differences in the peak shapes with the slight asymmetry of the azupyrene spectrum have been explained by the different molecular topologies.[26] The monolayer spectra of the two molecules show much larger differences, indicating their different interaction with the metal surface. For pyrene, the monolayer and multilayer signals are very similar regarding binding energy and peak shape, which remains symmetric. In contrast, the monolayer peak of azupyrene shows a strongly asymmetric tailing and is shifted by -0.25 eV with respect to the multilayer signal. The asymmetric peak shape can be explained by final state effects, which occur when density of states (DOS) close to the Fermi energy (E_F) is located at the corresponding atom,[40] indicating hybridization of molecular orbitals with metal states in the case of the model defect.

Second, the valence electronic structure was probed by UPS (Figure 4d). Monolayer pyrene causes partial attenuation of the surface state and a slight shift by 0.1 eV to lower binding energy, as is typical for flat-lying π-conjugated molecules physisorbed on metals. In contrast, monolayer azupyrene completely suppresses the surface state and causes increased intensity over the whole range between E_F and the copper d-band, confirming that the molecule-metal hybridization causes the asymmetry of the C1s peak of azupyrene (see above and Figure 4c). The photoemission data thus indicate that only the model defect azupyrene, but not pyrene, forms a chemisorptive bond to the copper surface. The bonding mechanism will be discussed below in the context of DFT analysis. The increased azupyrene-metal interaction is further confirmed by a larger work-function change (-1.18 eV for azupyrene and -0.86 eV for pyrene), as shown in the Supplementary Discussion.

Third, the unoccupied valence electronic structures were probed by NEXAFS spectroscopy. In Figure 5, the carbon K-edge NEXAFS spectra of multilayers (Figure 5a,b) and monolayers (Figure 5c,d) on Cu(111) are shown. The lower part of Figure 5 shows the corresponding MO-projected DFT NEXAFS calculations for both systems.[41] In the multilayer spectra, the π* and σ* resonances can clearly be distinguished. The onset of the first π* resonance appears at a lower photon energy for azupyrene than for pyrene, indicating a lower-lying LUMO of azupyrene. The dichroism of the monolayer spectra, especially the vanishing π* intensity at normal incidence, confirms that both molecules bind with the molecular plane parallel to the surface. The monolayer spectrum of pyrene taken with 25° incidence angle resembles the multilayer spectrum, with only slightly broadened π* resonances and some peak shifts at higher lying transitions, confirming the weak interaction with the metal surface. For azupyrene, the situation changes distinctly: Its interaction with the metal induces a massive decrease of overall intensity and a completely different peak shape for the first π* resonance. As the DFT calculations reveal, these changes are caused by reduced relative intensities attributed to the C1s→LUMO transition compared to the transitions into higher states.
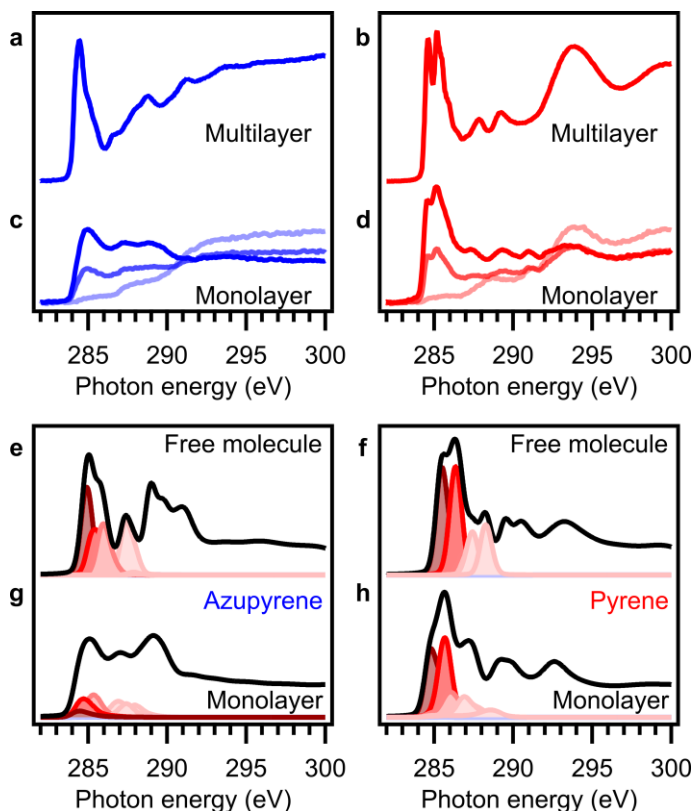
Figure 5. Carbon K-edge NEXAFS data reveal the interaction-induced changes in the unoccupied orbitals of the model defect azupyrene. Experimental spectra: (a,b) multilayers; (c,d) monolayers of (a,c) azupyrene and (b,d) pyrene. The multilayer spectra were taken with the electric field vector oriented 53° relative to the surface normal, while the monolayer spectra were taken with the angles indicated by the color scheme (25°, bold color; 53°, intermediate color; 90°, faint color). MO-projection analysis of the DFT-calculated NEXAFS spectra of the free molecules (e,f) and the monolayers (g,h). (e,g) azupyrene; (f,h) pyrene. Contributions of the LUMO in dark red and those of the higher orbitals in incrementally lighter colors; total spectrum in black. The calculated spectra were rigidly shifted by -6 eV to match the experimental energy scale.[28] The calculations for the free molecule were already published elsewhere.[26, 41]

Analysis of the defect/metal interaction. Periodic DFT calculations (with the D3 dispersion correction) provide a deeper understanding of the effects governing the different interactions of the model defect and its reference isomer with the copper surface. Structural information about the most favorable adsorption site of each molecule as determined by DFT is shown in Figure 3f-m. The adsorption sites are in good agreement with AFM (see Supplementary Figure S2).

DFT predicts adsorption distances of 2.43 Å (azupyrene) and 2.96 Å (pyrene), confirming the experimental finding that azupyrene binds much closer to the surface. While the pyrene/metal

interaction does not significantly affect the structure of the molecule and the surface (Figure 3i,k,m), azupyrene and the first Cu surface layer undergo substantial out-of-plane deformation (Figure 3h,j). The in-plane bond lengths of azupyrene are also affected: All perimeter bonds and the central bond are elongated, whereas the bonds connecting the central carbon atoms to the perimeter are shortened (Figure 3l). These changes result from electron donation into the LUMO, which has a nodal plane intersecting the elongated central bond, but bonding character with respect to the shortened bonds (see Figure 6 and Supplementary Figure S8). In the framework of aromaticity models, these changes correspond to a partial transition from a predominantly annulenoid conjugation along the perimeter in the free molecule to a more benzenoid conjugation in the adsorbed state (see Supplementary Discussion and Supplementary Figure S9).

Molecule-metal bond energies (adsorption energies) obtained by DFT calculations confirm that azupyrene forms the stronger bond to the metal surface. For a quantitative comparison with the TPD results, which requires a detailed discussion of the coverages and suitable integration of the TPD energies, see the Supplementary Discussion.

Profound insight into the surface chemical bond was gained by analysis of the interaction energies using the periodic energy decomposition analysis (pEDA) method with the natural orbitals for chemical valence (NOCV) extension.[42-44] The pEDA method divides the interaction energy between two fragments (here: surface and molecule) into physically well-defined terms. The NOCV extension then pinpoints specific orbital interactions as constituents of the analyzed bond. This analysis shows that azupyrene forms a chemical bond to the surface, which is characterized by charge transfer from the surface to the molecule's LUMO (and, to lesser extent, the LUMO+1), in line with the NEXAFS results. In contrast, pyrene shows only physisorptive interaction, dominated by dispersion interactions and an even positive electronic interaction term. A more detailed discussion of the pEDA results and the corresponding convergence calculations is provided in the Supplementary Discussion, Supplementary Tables S3 to S6 and Supplementary Figure S8. The pEDA agrees with the overall charge density difference due to the adsorption, which is presented in the form of charge density difference plots (Figure 6a-d). These show electron accumulation in the shape of the former LUMO for azupyrene (Figure 6a,b), whereas for pyrene no significant charge transfer is visible (Fig 6c,d). The electronic density of states for the carbon atoms (Figure 6e) shows the substantial hybridisation of the azupyrene orbitals with the metal states of the surface, leading to a significant DOS around E_F (in agreement with the UPS data), while pyrene shows a clear band gap.

To quantify the charge transfer at the molecule-metal interface, several charge partitioning schemes were employed. While the magnitude of the charge transfer is dependent on the method and varies substantially, all methods consistently show an appreciable charge transfer for azupyrene (up to 1.40 e) and only a minor charge transfer (less than 0.2 e) for pyrene (see Supplementary Tab. S1). This confirms the trend seen for the embedded defects (Figure 2),

where substantial localized charge transfer around the defect was found. For comparison between the molecular model systems (including azulene as model for the 5-7 defect[28]) and the graphene-embedded defects, it is necessary to consider the molecule-metal bonding distances (heights). While the model defects are free to optimize their heights, the heights of the embedded defects are partly influenced by the surrounding ideal graphene network. If the model molecules are lifted from their equilibrium height to the adsorption height of the ideal graphene layer, the charge transfer (according to the iterative Hirshfeld partitioning scheme) is reduced from -0.19 e to -0.04 e for pyrene and from -0.66 e to -0.15 e for azupyrene. Still, a notable charge transfer remains for azupyrene, which is identical to the charge transfer occurring locally at the embedded S-W defect site of also 0.15 e (see Supplementary Tab. S1 for details and other charge portioning schemes).
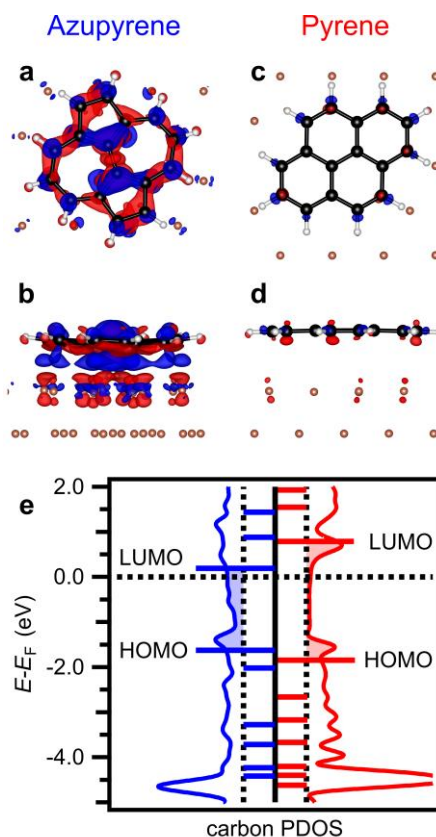

Figure 6. DFT-based bonding analysis shows electron transfer from the Cu(111) surface into the unoccupied LUMO of azupyrene and no charge transfer for pyrene**.** (a-d) Charge density difference plots for azupyrene (a,b) and pyrene (c,d). The iso surface value is 0.002 e$^-$/Å^3 for all plots. Red, electron depletion; blue, electron accumulation. (e) Carbon-projected density of states of the azupyrene (left) and pyrene (right), horizontal lines indicate the gas phase orbital energies, shifted to account for the work function. Subfigures (a,b) show similarity to the electron rearrangement surrounding the S-W defect (see Figure 2e,h).

Using the partial charges for the graphene systems, we are now able prove that the charge transfer at the graphene/metal interface is localized at the defect sites, as was already suggested by the charge density difference plots in Figure 2d-i. This is achieved by summations over the partial charges for different local groups of atoms around the defect site and for the whole unit cell, as shown in the Supplementary Tab. S2 for both the S-W and the 5-7 defect. The strong localization of the metal/defect interaction provides a final justification for our approach to study monolayers of molecular model defects.

Conclusions

Topological defects in graphene, such as the S-W defect, cause enhanced bonding at the graphene/metal interface, as revealed by increased bond energies, reduced bond distances, and enhanced charge transfer. The defect-mediated graphene/metal bonding mechanism, which is clarified by DFT for the embedded defects, is corroborated using molecular model systems. Experimentally, the bond between a copper surface and the model S-W defect is stronger by 52% (68 kJ/mol) and shorter by 0.9 Å, compared to the reference model for ideal graphene. Spectroscopic data show that the model defect's electronic states hybridize with those of the metal and that LUMO and LUMO+1 become partly occupied, as is confirmed by DFT. The agreement between the theoretically predicted influences of defects on extended graphene/metal interfaces and the experimental and theoretical findings for the molecular defect models show that the latter are suitable for obtaining experimental information that is inaccessible for embedded defects. The defect-induced enhanced electronic coupling at graphene/metal contacts is expected to affect the performance of graphene-based (opto)electronic devices, *e.g.* by increasing charge injection rates, suggesting performance control through topological engineering. Using other nonalternant and nonbenzenoid nanographenes as model systems, the here applied methodology can be expanded to other types of defects and thereby contribute to a realistic picture of graphene/metal contacts. Further work should be devoted to other metals that are commonly used for contacting graphene, such as gold or titanium, and to polycrystalline materials.

Methods

Experimental Methods. The adsorption of azupyrene and pyrene on Cu(111) was studied under ultra-high vacuum (UHV) conditions at base pressures below 2×10^{-10} mbar.

The detailed synthesis procedure of azupyrene (dicyclopenta[ef,kl]heptalene) is described in detail in a previous publication.[26] Azupyrene and pyrene (Sigma-Aldrich, purity >99 %) were deposited onto the substrate with a home-build line-of-sight evaporator after initial pump-freeze-thaw cycles of the reservoirs. The polished Cu(111) single-crystal surface (purity >99.999 %, roughness <0.01 µm, orientation accuracy <0.4°, from MaTecK/Germany) was prepared by iterated cycles of sputtering with Ar^+ ions (1 keV, 15 µA, 30 min) and annealing

(800-830 K, 15 min). Surface cleanliness and structure were confirmed by XPS, LEED and STM. Sample temperatures were measured with a type K thermocouple directly mounted to the single crystal. Coverages are given in the unit monolayer (ML) according one complete layer of molecules on the surface. For pyrene on Cu(111) the complete monolayer is formed by a (4×4) structure corresponding to 0.063 molecules per first layer Cu atom, for azupyrene the monolayer is formed by a more dense ($\sqrt{13}\times\sqrt{13}$) structure (0.077 molecules per Cu atom).

TPD measurements were performed with a HIDEN EPIC 1000 mass spectrometer mounted inside a differentially pumped cryoshroud for line-of-sight mass spectrometry.

The LT-AFM measurements were performed with a commercial low temperature atomic force microscope (ScientaOmicron, Germany). The temperature during the AFM measurements was about 5.2 K, the base pressure in the chamber is below $1\cdot10^{-10}$ mbar. All images and measurements were obtained with a CO-terminated tip. The q-plus tuning fork sensor[45] had a resonance frequency of $f_{res} \approx 25.6$ kHz, a quality factor of $Q \approx 30000$ and an oscillation amplitude of $A \approx 70$ pm. During the AFM constant-height measurements a small gap voltage of -0.54 mV was applied to the sample to compensate the voltage offset of the tunneling amplifier.

XPS and UPS were performed with a PHOIBOS 150 electron energy analyzer equipped with an MCD-9 multi channeltron detector. For XPS, monochromatic Al-K$_\alpha$ radiation from a SPECS XR 50 M X-ray anode with a FOCUS 500 monochromator was employed. He-II UP spectra and work functions were measured with a UVS 10/35 gas discharge source and the same analyzer set up.

NEXAFS spectroscopy was performed at the synchrotron radiation facility BESSY II (Helmholtz-Zentrum Berlin) using the HE-SGM dipole beamline, the partial electron-yield (PEY) mode was used with a retarding field of -150 V and a channeltron detector voltage of 2.3 keV. The thus obtained NEXAFS data was treated as described previously.[28]

Density Functional Theory Calculations. Periodic density-functional-theory calculations were performed using the Vienna Ab Initio Simulation Package (VASP)[46] while employing the generalized gradient approximation (GGA) functional proposed by Perdew, Burke, and Ernzerhof (PBE)[47] in combination with the D3 van-der-Waals correction scheme with Becke-Johnson damping.[48-49] and the projector-augmented wave (PAW) ansatz[50-51] for the atomic cores. A plane-wave cutoff energy of 350 eV, a vacuum layer of 30 Å and a 6×6×1 Monkhorst Pack k-point grid were chosen, which has been validated in previous studies on similar systems.[28-30] NEXAFS calculations were performed with the code CASTEP-18.1,[52] using the ELNES[53] module. Transition energies and intensities were obtained with the ΔIP-TP method.[41, 54] Further technical details of the calculations can be found in the Supplementary Methods.

Associated Content

Supporting Information

The Supporting Information is available free of charge at https://pubs.acs.org/XXX. Additional data and discussion for the nc-AFM, XPS, UPS, and TPD measurements. HOMA analysis, the detailed pEDA discussion and miscellaneous technical details of the DFT calculations. Data and metadata are openly available at data_UMR Research Data Repository under a CC-BY 4.0 license (https://doi.org/10.17192/fdr/102).

Author Information

Corresponding Authors

Prof. Dr. J. Michael Gottfried
*michael.gottfried@chemie.uni-marburg.de

Prof. Dr. Andre Schirmeisen
*andre.schirmeisen@ap.physik.uni-giessen.de

Notes

The authors declare no competing interests.

Acknowledgments

References

1. Geim, A. K.; Novoselov, K. S., The rise of graphene. *Nat. Mater.* **2007,** *6*, 183-191.
2. Kim, P., Across the border. *Nat. Mater.* **2010,** *9*, 792-793.
3. Hashimoto, A.; Suenaga, K.; Gloter, A.; Urita, K.; Iijima, S., Direct evidence for atomic defects in graphene layers. *Nature* **2004,** *430*, 870-873.
4. Kotakoski, J.; Krasheninnikov, A. V.; Kaiser, U.; Meyer, J. C., From Point Defects in Graphene to Two-Dimensional Amorphous Carbon. *Phys. Rev. Lett.* **2011,** *106*, 105505.
5. Meyer, J. C.; Kisielowski, C.; Erni, R.; Rossell, M. D.; Crommie, M. F.; Zettl, A., Direct Imaging of Lattice Atoms and Topological Defects in Graphene Membranes. *Nano Lett.* **2008,** *8*, 3582-3586.
6. Tsen, A. W.; Brown, L.; Levendorf, M. P.; Ghahari, F.; Huang, P. Y.; Havener, R. W.; Ruiz-Vargas, C. S.; Muller, D. A.; Kim, P.; Park, J., Tailoring Electrical Transport Across Grain Boundaries in Polycrystalline Graphene. *Science* **2012,** *336*, 1143-1146.
7. Huang, P. Y.; Ruiz-Vargas, C. S.; van der Zande, A. M.; Whitney, W. S.; Levendorf, M. P.; Kevek, J. W.; Garg, S.; Alden, J. S.; Hustedt, C. J.; Zhu, Y.; Park, J.; McEuen, P. L.; Muller, D. A., Grains and grain boundaries in single-layer graphene atomic patchwork quilts. *Nature* **2011,** *469*, 389-393.
8. Kim, K.; Lee, Z.; Regan, W.; Kisielowski, C.; Crommie, M. F.; Zettl, A., Grain Boundary Mapping in Polycrystalline Graphene. *ACS Nano* **2011,** *5*, 2142-2146.
9. Rasool, H. I.; Ophus, C.; Klug, W. S.; Zettl, A.; Gimzewski, J. K., Measurement of the intrinsic strength of crystalline and polycrystalline graphene. *Nat. Commun.* **2013,** *4*, 2811.
10. Ito, Y.; Shen, Y.; Hojo, D.; Itagaki, Y.; Fujita, T.; Chen, L.; Aida, T.; Tang, Z.; Adschiri, T.; Chen, M., Correlation between Chemical Dopants and Topological Defects in Catalytically Active Nanoporous Graphene. *Adv. Mater.* **2016,** *28*, 10644-10651.
11. Malola, S.; Häkkinen, H.; Koskinen, P., Structural, chemical, and dynamical trends in graphene grain boundaries. *Phys. Rev. B* **2010,** *81*, 165447.
12. Grantab, R.; Shenoy, V. B.; Ruoff, R. S., Anomalous Strength Characteristics of Tilt Grain Boundaries in Graphene. *Science* **2010,** *330*, 946-948.
13. Wei, Y.; Wu, J.; Yin, H.; Shi, X.; Yang, R.; Dresselhaus, M., The nature of strength enhancement and weakening by pentagon-heptagon defects in graphene. *Nat. Mater.* **2012,** *11*, 759-763.
14. Shekhawat, A.; Ritchie, R. O., Toughness and strength of nanocrystalline graphene. *Nat. Commun.* **2016,** *7*, 10546.
15. Yazyev, O. V.; Louie, S. G., Electronic transport in polycrystalline graphene. *Nat. Mater.* **2010,** *9*, 806-809.
16. Cervenka, J.; Katsnelson, M. I.; Flipse, C. F. J., Room-temperature ferromagnetism in graphite driven by two-dimensional networks of point defects. *Nat. Phys.* **2009,** *5*, 840-844.
17. Ni, B.; Zhang, T.; Li, J.; Li, X.; Gao, H., Topological Design of Graphene. In *Handbook of Graphene Set*, Celasco, E.; Chaika, A. N.; Stauber, T.; Zhang, M.; Ozkan, C.; Ozkan, C.; Ozkan, U.; Palys, B.; Harun, S. W., Eds. Wiley: New York, 2019.
18. Sun, Y.; Sun, M.; Xie, D., 5 - Graphene Electronic Devices. In *Graphene*, Zhu, H.; Xu, Z.; Xie, D.; Fang, Y., Eds. Academic Press, Cambridge: 2018; pp 103-155.
19. Wang, R.; Ren, X.-G.; Yan, Z.; Jiang, L.-J.; Sha, W. E. I.; Shan, G.-C., Graphene based functional devices: A short review. *Front. Phys.* **2019,** *14*, 13603.
20. Cusati, T.; Fiori, G.; Gahoi, A.; Passi, V.; Lemme, M. C.; Fortunelli, A.; Iannaccone, G., Electrical properties of graphene-metal contacts. *Sci. Rep.* **2017,** *7*, 5109.
21. Giovannetti, G.; Khomyakov, P. A.; Brocks, G.; Karpan, V. M.; van den Brink, J.; Kelly, P. J., Doping Graphene with Metal Contacts. *Phys. Rev. Lett.* **2008,** *101*, 026803.

22. Banhart, F.; Kotakoski, J.; Krasheninnikov, A. V., Structural Defects in Graphene. *ACS Nano* **2011,** *5*, 26-41.

23. Chen, D.; Zheng, Y.; Liu, L.; Zhang, G.; Chen, M.; Jiao, Y.; Zhuang, H., Stone–Wales defects preserve hyperuniformity in amorphous two-dimensional networks. *Proc. Natl. Acad. Sci.* **2021,** *118*, e2016862118.

24. Suenaga, K.; Wakabayashi, H.; Koshino, M.; Sato, Y.; Urita, K.; Iijima, S., Imaging active topological defects in carbon nanotubes. *Nat. Nanotech.* **2007,** *2*, 358-360.

25. Mallion, R. B.; Rouvray, D. H., The Golden Jubilee of the Coulson-Rushbrooke Pairing Theorem. *J. Math. Chem.* **1990,** *5*, 1-21.

26. Klein, B. P.; Ruppenthal, L.; Hall, S. J.; Sattler, L. E.; Weber, S. M.; Herritsch, J.; Jaegermann, A.; Maurer, R. J.; Hilt, G.; Gottfried, M., Topology Effects in Molecular Organic Electronic Materials: Pyrene and Azupyrene. *ChemPhysChem* **2021,** *22*, 1065-1073.

27. Xin, H.; Gao, X., Application of Azulene in Constructing Organic Optoelectronic Materials: New Tricks for an Old Dog. *ChemPlusChem* **2017,** *82*, 945-956.

28. Klein, B. P.; van der Heijden, N. J.; Kachel, S. R.; Franke, M.; Krug, C. K.; Greulich, K. K.; Ruppenthal, L.; Müller, P.; Rosenow, P.; Parhizkar, S.; Bocquet, F. C.; Schmid, M.; Hieringer, W.; Maurer, R. J.; Tonner, R.; Kumpf, C.; Swart, I.; Gottfried, J. M., Molecular Topology and the Surface Chemical Bond: Alternant Versus Nonalternant Aromatic Systems as Functional Structural Elements. *Phys. Rev. X* **2019,** *9*, 011030.

29. Klein, B. P.; Morbec, J. M.; Franke, M.; Greulich, K. K.; Sachs, M.; Parhizkar, S.; Bocquet, F. C.; Schmid, M.; Hall, S. J.; Maurer, R. J.; Meyer, B.; Tonner, R.; Kumpf, C.; Kratzer, P.; Gottfried, J. M., Molecule-Metal Bond of Alternant versus Nonalternant Aromatic Systems on Coinage Metal Surfaces: Naphthalene versus Azulene on Ag(111) and Cu(111). *J. Phys. Chem. C* **2019,** *123*, 29219-29230.

30. Kachel, S. R.; Klein, B. P.; Morbec, J. M.; Schöniger, M.; Hutter, M.; Schmid, M.; Kratzer, P.; Meyer, B.; Tonner, R.; Gottfried, J. M., Chemisorption and Physisorption at the Metal/Organic Interface: Bond Energies of Naphthalene and Azulene on Coinage Metal Surfaces. *J. Phys. Chem. C* **2020,** *124*, 8257-8268.

31. Klein, B. P.; Harman, S. E.; Ruppenthal, L.; Ruehl, G. M.; Hall, S. J.; Carey, S. J.; Herritsch, J.; Schmid, M.; Maurer, R. J.; Tonner, R.; Campbell, C. T.; Gottfried, J. M., Enhanced Bonding of Pentagon–Heptagon Defects in Graphene to Metal Surfaces: Insights from the Adsorption of Azulene and Naphthalene to Pt(111). *Chem. Mater.* **2020,** *32*, DOI: 10.1021/acs.chemmater.9b03744.

32. Chanier, T.; Henrard, L., From carbon atom to graphene on Cu(111): an ab-initio study. *Eur. Phys. J. B* **2015,** *88*, 5.

33. Zhong, Q.; Ebeling, D.; Tschakert, J.; Gao, Y.; Bao, D.; Du, S.; Li, C.; Chi, L.; Schirmeisen, A., Symmetry breakdown of 4,4''-diamino-p-terphenyl on a Cu(111) surface by lattice mismatch. *Nat. Commun.* **2018,** *9*, 3277.

34. Schuler, B.; Liu, W.; Tkatchenko, A.; Moll, N.; Meyer, G.; Mistry, A.; Fox, D.; Gross, L., Adsorption Geometry Determination of Single Molecules by Atomic Force Microscopy. *Phys. Rev. Lett.* **2013,** *111*, 106103.

35. Nieskens, D. L. S.; van Bavel, A. P.; Niemantsverdriet, J. W., The analysis of temperature programmed desorption experiments of systems with lateral interactions; implications of the compensation effect. *Surf. Sci.* **2003,** *546*, 159-169.

36. King, D. A., Thermal desorption from metal surfaces: A review. *Surf. Sci.* **1975,** *47*, 384-402.

37. Witte, G.; Lukas, S.; Bagus, P. S.; Wöll, C., Vacuum level alignment at organic/metal junctions: "Cushion" effect and the interface dipole. *Appl. Phys. Lett.* **2005,** *87*, 263502.

38. Tait, S. L.; Dohnálek, Z.; Campbell, C. T.; Kay, B. D., n-alkanes on MgO(100). I. Coverage-dependent desorption kinetics of n-butane. *J. Chem. Phys.* **2005,** *122*, 164707.

39. Pecher, J.; Tonner, R., Precursor states of organic adsorbates on semiconductor surfaces are chemisorbed and immobile. *ChemPhysChem* **2017,** *18*, 34-38.

40. Doniach, S.; Sunjic, M., Many-electron singularity in X-ray photoemission and X-ray line spectra from metals. *J. Phys. C: Solid State Phys.* **1970,** *3*, 285-291.

41. Klein, B. P.; Hall, S. J.; Maurer, R. J., The nuts and bolts of core-hole constrained ab initio simulation for K-shell x-ray photoemission and absorption spectra. *J. Phys.: Condens. Matt.* **2021,** *33*, 154005.

42. Raupach, M.; Tonner, R., A periodic energy decomposition analysis method for the investigation of chemical bonding in extended systems. *J. Chem. Phys.* **2015,** *142*, 194105.

43. Mitoraj, M. P.; Michalak, A.; Ziegler, T., A Combined Charge and Energy Decomposition Scheme for Bond Analysis. *J. Chem. Theory Comput.* **2009,** *5*, 962-975.

44. Pecher, L.; Tonner, R., Deriving bonding concepts for molecules, surfaces, and solids with energy decomposition analysis for extended systems. *WIREs Comput Mol Sci.* **2019,** *9*, e1401.

45. Giessibl, F. J., High-speed force sensor for force microscopy and profilometry utilizing a quartz tuning fork. *Appl. Phys. Lett.* **1998,** *73*, 3956-3958.

46. Kresse, G.; Hafner, J., Ab initio molecular dynamics for liquid metals. *Phys. Rev. B* **1993,** *47*, 558-561.

47. Perdew, J. P.; Burke, K.; Ernzerhof, M., Generalized Gradient Approximation Made Simple. *Phys. Rev. Lett.* **1996,** *77*, 3865-3868.

48. Grimme, S.; Antony, J.; Ehrlich, S.; Krieg, H., A consistent and accurate ab initio parametrization of density functional dispersion correction (DFT-D) for the 94 elements H-Pu. *J. Chem. Phys.* **2010,** *132*, 154104.

49. Becke, A. D.; Johnson, E. R., A density-functional model of the dispersion interaction. *J. Chem. Phys.* **2005,** *123*, 154101.

50. Blöchl, P. E., Projector augmented-wave method. *Phys. Rev. B* **1994,** *50*, 17953-17979.

51. Kresse, G.; Joubert, D., From ultrasoft pseudopotentials to the projector augmented-wave method. *Phys. Rev. B* **1999,** *59*, 1758-1775.

52. Clark, S. J.; Segall, M. D.; Pickard, C. J.; Hasnip, P. J.; Probert, M. I. J.; Refson, K.; Payne, M. C., First principles methods using CASTEP. *Z. Kristallogr. Cryst. Mater.* **2005,** *220*, 567–570.

53. Mizoguchi, T.; Tanaka, I.; Gao, S.-P.; Pickard, C. J., First-principles calculation of spectral features, chemical shift and absolute threshold of ELNES and XANES using a plane wave pseudopotential method. *J. Phys.: Condens. Matter* **2009,** *21*, 104204.

54. Triguero, L.; Pettersson, L. G. M.; Ågren, H., Calculations of near-edge x-ray-absorption spectra of gas-phase and chemisorbed molecules by means of density-functional and transition-potential theory. *Phys. Rev. B* **1998,** *58*, 8097-8110.

TOC Graphic